Microkinetic Mechanisms for Partial Oxidation of Methane over Platinum and Rhodium

P. Kraus and R. P. Lindstedt*

Department of Mechanical Engineering, Imperial College, Exhibition Road, London SW7 2AZ, UK

E-mail: p.lindstedt@imperial.ac.uk

*To whom correspondence should be addressed

Abstract

A systematic approach for the development of heterogeneous mechanisms is applied and evaluated for the catalytic partial oxidation of methane over platinum (Pt) and rhodium (Rh). The derived mechanisms are self-consistent and based on a reaction class-based framework comprising variational transition state theory (VTST) and two-dimensional collision theory for the calculation of pre-exponential factors with barrier heights obtained using the unity bond index – quadratic exponential potential (UBI–QEP) method. The surface chemistry is combined with a detailed chemistry for the gas phase and the accuracy of the approach is evaluated over Pt for a wide range of stoichiometries ($0.3 \leq \phi \leq 4.0$), pressures ($2 \leq$ P (bar) ≤ 16) and residence times. It is shown that the derived mechanism can reproduce experimental data with an accuracy comparable to the prevalent collision theory approach and without the reliance on experimental data for sticking coefficients. The derived mechanism for Rh shows encouraging agreement for a similar set of conditions and the robustness of the approach is further evaluated by incorporating partial updates via more accurate DFT determined barrier heights. Substantial differences are noted for some channels (e.g. where reaction progress is strongly influenced by early transition states) though the impact on the overall agreement with experimental data is moderate for the current systems. Remaining discrepancies are explored using sensitivity analyses to establish key parameters. The study suggests that the overall framework is well–suited for the efficient generation of heterogeneous reaction mechanisms, that it can serve to identify key parameters where high accuracy *ab initio* methods are required and that it permits the inclusion of such updates as part of a gradual refinement process.

1 Introduction

Following the development of the Fischer-Tropsch process,[1] methane is an increasingly important feedstock for the production of fine chemicals. Traditionally, methane has been reformed to syngas using steam over a nickel catalyst[2,3] requiring a large amount of energy. The majority of the current hydrogen demand is met with this method,[4] which is essentially the reverse of the Sabatier reduction, which won a Nobel Prize in 1912.[5] Methane is currently mainly obtained from natural gas.[6,7] However, renewable sources have been developed[8,9] to provide a green pathway from biomass to synthetic fuels, alcohols and light alkenes.[10]

The catalytic partial oxidation (CPO) of methane is an alternative to steam reforming that was first proposed by Liander.[11] The CPO approach has many benefits over traditional steam reforming: it is auto–thermal and therefore energy–saving, and produces syngas with

a H_2/CO ratio ideal for a subsequent Fischer-Tropsch synthesis.[12] Various catalytic materials for methane oxidation have been developed, including traditional and noble metal catalysts.[13] The thermodynamic and mechanistic aspects of the process have been recently reviewed.[12,14] Dry reforming of methane, using CO_2 co-feed instead of O_2 (in partial oxidation) or H_2O (in steam reforming) presents an alternative approach with the benefit of using of otherwise polluting CO_2. However, the process is energy intensive and susceptible to carbon deposition.[12,15] The chemistry remains conjectural for some aspects of these systems and the coupling with the gas phase results in further uncertainties.

Kraus and Lindstedt[16,17] proposed a class-based framework for the development of heterogeneous reaction mechanisms based on the method of Vincent et al.[18] The latter approach used two-dimensional collision theory[19] to calculate pre-exponential factors and the unity bond index – quadratic exponential potential (UBI–QEP) method[20] to obtain barrier heights. Hence, the calculation of pre-exponential factors required experimentally-derived sticking coefficients, which can vary by orders of magnitude even comparably simple systems, such as H_2 on Pt surfaces,[21–23] while a successful experimental determination for reactive intermediates remains extremely challenging. Kraus and Lindstedt[16] introduced a variational transition state theory (VTST) method to eliminate this requirement for the purposes of microkinetic modelling. The approach was successfully validated for hydrogen and syngas,[16] and ethane[17] combustion over platinum (Pt). The current work extends the assessment and robustness of the approach by (i) considering the CPO of methane for the CH_4/O_2/Pt system, (ii) the investigation of rhodium-based catalysis for the CH_4/O_2/Rh system and (iii) the potential for the inclusion of more accurate density functional theory (DFT) based data to provide partial updates. The performance of the approach is assessed over a wide range of stoichiometries ($0.3 \leq \phi \leq 4.0$), pressures ($2 \leq$ P (bar) ≤ 16) and residence times. It is also shown that (iv) the current systematic approach can serve as a basis for the identification of key reaction channels where high accuracy *ab initio* methods are beneficial.

2 Data set selection

The recent literature on CH_4 combustion over Pt includes stagnation flow studies with H_2 co–feed,[24] and as an additive in H_2/O_2 combustion.[25] The studies include the validation of the CH_4/O_2/Pt mechanisms of Deutschmann et al.[24] and Zerkle et al.,[26] while Mantzaras et al.[27] studied the ignition behaviour of fuel lean mixtures using parabolic and elliptical calculation methods and compared with experimental data. Recent experimental investigations include the study of methane conversion over Pt–based catalysts with alumina,[28] ceria and zirconia supports[29] and a comparison of methane, methanol and ethanol reforming over Pt/ZSM–5 at various stoichiometries.[30] The effect of oxygen coverage on methane activation was investigated by Weng et al.[10] using Pt and palladium (Pd) catalysts. The amount of previous work on methane oxidation over Pt suggests that the system is well suited for the current study of the accuracy of methods for the generation of heterogeneous reactions mechanisms. In addition, rhodium (Rh) was included for the following reasons:

- Rh has a very high activity[12,31] and good performance in CPO of CH_4.[14,32]
- Rh belongs to a different group of elements (second row transition metal) corresponding to a different number of valence electrons.
- Experimental studies performed under comparable conditions and using similar geometries are available for both Pt and Rh.

The literature on Rh based catalytic reforming is also comparably rich. Enger et al.[14] reviewed earlier work on partial oxidation and Pakhare and Spivey[15] covered dry reforming. More recent experimental and computational work on dry reforming was presented by Nematollahi et al.[33] and the impact of catalytic supports was studied by Drif et al.[34] A three-dimensional simulation of a packed bed reactor was performed by Wehinger et al.[35]

Recent developments in partial oxidation include the extension of the detailed mechanism of Deutschmann et al.[36–38] for H_2/O_2 combustion to syngas and methane.[36] The development

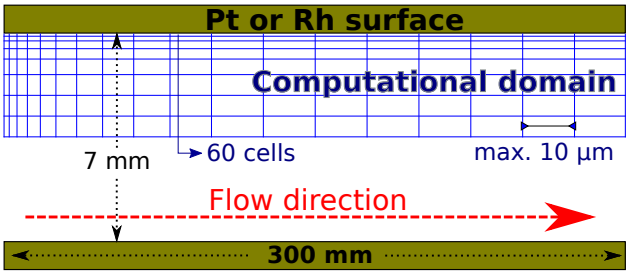

Figure 1: A diagram of the computational domain overlaid over the outline of the experimental configuration at the Paul Scherrer Institute.[42–45]

of the mechanism was based on experimental data from the stagnation flow configuration of Karadeniz et al.[37] Validation was also performed against experimental data covering the effect of inlet temperature on catalyst stability and outlet composition.[38,39] Recent DFT studies include detailed energetics of CO, C_2 and oxygenated compounds[40] and the impact of surface coordination on product selectivity on various Rh surfaces.[41]

The experimental data sets selected for validation provide a consistent treatment for Pt and Rh catalysts and feature a subset of the conditions investigated using a high-pressure chamber.[42–45] The corresponding computational domain is shown in Fig. 1. The datasets for Pt include five cases of fuel-lean combustion by Reinke et al.[42] and two cases of CPO of methane also at elevated pressure by Sui et al.[45] The experimental data sets selected for Rh comprise four cases of fuel-lean conditions from Sui et al.[44] and five cases featuring CPO of methane by Appel et al.[43] and Sui et al.[45] The experimental conditions are presented in Table 1 for Pt and Table 2 for Rh.

3 Computational methods

The computations were performed using a two-dimensional parabolic (boundary layer) code with the conservation equations for mass, momentum, species mass fractions (Y_k) and enthalpy (h) shown below, where the velocity components are denoted u and v for the x (axial) and y (transverse) directions respectively. Additionally, ρ is the density of the fluid, C_p is the specific heat capacity at constant pressure, μ is the viscosity, λ is the thermal conductivity,

n is the mole number (molality) and P is the pressure. A gas phase species i is characterised by its enthalpy h_i, molar mass M_i, diffusion coefficient D_i, diffusive flux J_i and net formation rate R_i. Finally, v_C is a correction velocity, chosen so that the sum of all fluxes is zero at the cell interfaces as outlined by Jones and Lindstedt.[46]

$$
\begin{aligned}
\frac{\partial(\rho u)}{\partial x} + \frac{\partial(\rho v)}{\partial y} &= 0 \\
\rho u \frac{\partial Y_i}{\partial x} + \rho v \frac{\partial Y_i}{\partial y} &= -\frac{\partial(J_i)}{\partial y} + M_i R_i \\
\rho u \frac{\partial u}{\partial x} + \rho v \frac{\partial u}{\partial y} &= -\frac{\partial P}{\partial x} + \frac{\partial}{\partial y}\left(\mu \frac{\partial u}{\partial y}\right) \\
\rho u \frac{\partial h}{\partial x} + \rho v \frac{\partial h}{\partial y} &= \frac{\partial}{\partial y}\left(\frac{\lambda}{C_p}\frac{\partial h}{\partial y}\right) + \frac{\partial}{\partial y}\left[\sum^{i \to N_g} h_i \cdot \left(-J_i - \frac{\lambda}{C_p}\frac{\partial Y_i}{\partial y}\right)\right] \\
-J_i &= \rho D_i \left(\frac{\partial Y_i}{\partial y} - Y_i \frac{1}{n}\frac{\partial n}{\partial y}\right) - \rho v_C Y_i
\end{aligned}
$$

The above equations were solved in a transformed stream function based coordinate system as outlined by Spalding.[47] The non-dimensional $x-\omega$ form of the governing equations is preferred as direct use of the von Mises transformation can be problematic.[48] An implicit discretisation scheme, featuring two-point backward differencing for the x–direction and central differencing for the cross-stream (y–) direction, was used.[46]

The surface and gas phase chemistries are coupled according to Coltrin et al.[49] by balancing the species flux at the gas–wall interface with the mass-weighted production rate at the catalytic wall $J_i + \rho Y_i v_s = R_i M_i$, where v_s is the Stephan velocity ($v_s = \frac{1}{\rho}\sum^{i \to N_g} R_i M_i$).[17,49,50] The resulting system of algebraic equations is highly nonlinear and a Newton linearisation, featuring an analytical evaluation of the derivatives, was utilised for the source term.[46] The resulting method is computationally stable and results in an efficient block tri-diagonal matrix structure. Alternative suggestions for the solution of the boundary layer equations have been formulated by Coltrin et al.[51] and Raja et al.[52] However, the current approach remains computationally efficient and has been used in a number of related studies.[16–18,53]

Table 1: Experimental conditions for Pt catalysed methane oxidation cases:[42,45] inlet stoichiometry, inlet velocity $\mathbf{U}_{in}^{\mathbf{T}_{in}}$, gas and wall temperatures at the inlet $\mathbf{T}_{in}$ and $\mathbf{T}_{in}^{W}$, inlet pressure $\mathbf{P}_{in}$. Catalyst site density $\Gamma = 27$ μmol/m^2 in all cases.

Case	ϕ	$\mathbf{U}_{in}^{\mathrm{T}_{in}}$ [m/s]	$\mathbf{T}_{in}$ [K]	$\mathbf{T}_{in}^{W}$ [K]	$\mathbf{P}_{in}$ [bar]
R01[42]	0.40	2.05	624	913	4
R08[42]	0.40	0.40	621	904	10
R06[42]	0.35	1.15	627	1040	7
R13[42]	0.35	0.55	606	901	14
R15[42]	0.35	0.46	592	834	16
Pt1[45]	1.80	0.47	426	1114	5
Pt3[45]	3.00	0.28	440	1051	5

Table 2: Experimental conditions for Rh catalysed methane oxidation cases:[43–45] inlet stoichiometry, inlet velocity $\mathbf{U}_{in}^{\mathbf{T}_{in}}$, gas and wall temperatures at the inlet $\mathbf{T}_{in}$ and $\mathbf{T}_{in}^{W}$, inlet pressure $\mathbf{P}_{in}$. Catalyst site density $\Gamma = 26$ μmol/m^2 in all cases.

Case	ϕ	$\mathbf{U}_{in}^{\mathrm{T}_{in}}$ [m/s]	$\mathbf{T}_{in}$ [K]	$\mathbf{T}_{in}^{W}$ [K]	$\mathbf{P}_{in}$ [bar]
S01[44]	0.30	1.25	395	779	2
S02[44]	0.38	1.26	392	799	2
S03[44]	0.33	0.41	437	882	5
S04[44]	0.40	0.50	387	790	5
Rh1[45]	1.80	0.47	429	1080	5
Rh3[45]	3.00	0.28	439	1052	5
A01[43]	4.00	0.30	395	1006	4
A02[43]	4.00	0.19	385	993	6
A03[43]	2.50	0.21	419	1054	6

The derivations for the extended case of turbulent boundary layers, including the current coordinate transformation, can also be found elsewhere[54] (see Appendices A–C).

The computational domain corresponds to the top half of the reactor, as shown in Fig. 1, with a symmetry condition applied at the centre line. The domain is resolved using 60 cells in the transverse direction with a geometrical scaling providing a resolution of 10 μm at the catalytic wall. The axial step is limited to 10 μm. The wall temperature is imposed from experimental data for all cases and assumed to account for non-adiabaticity effects. The catalytic site density Γ is set to a monolayer of Pt and Rh for all cases, corresponding to 27 and 26 μmol/m^2 respectively.

3.1 Gas phase chemistry

A C_1–C_2 subset of a revised gas phase mechanism of Lindstedt and Waldheim[55] (L+W) has been implemented in this study. The main changes compared to the previously validated mechanism of Lindstedt and Skevis[56] (L+S), used by Vincent et al.,[18] include modifications to the H_2/O_2 submechanism and adjustments to selected rates in the C_1 chemistry. The latter remain predominantly based on the work by the CEC data evaluation group of Baulch et al.[57,58] However, selected rates have been updated following the studies by Quiceno et al.,[59] Carl et al.[60] and Klippenstein et al.[61] The currently applied H_2/O_2 chemistry corresponds to the model of Burke et al.[62] The impact of the updated gas phase chemistry is discussed below in the context of assessing overall system sensitivities. The revised mechanism comprises 44 gas phase species and 270 reversible reactions, and is available in the Supporting information. Selected cases featuring combustion over Pt were also computed with the gas phase mechanism of Lindstedt and Skevis,[56] as it was used in previous work.[16–18]

3.2 Platinum surface chemistry

Two platinum surface mechanisms are applied *verbatim* in the current work, with the reaction class-based mechanism of Vincent et al.[18] compared to the corresponding VTST based mechanism of Kraus and Lindstedt.[17] While the formation of C_2 surface species is not expected under the currently studied conditions, the calculations have been performed with all C_2 pathways for consistency with previous work.[17]

3.3 Rhodium surface chemistry

Two rhodium mechanisms have been derived in the current work. The first is a systematically derived, VTST based, heterogeneous mechanism, formulated analogously to the Pt mechanism of Kraus and Lindstedt.[17] The approach is comparatively straightforward and

Table 3: Comparison of the treatment of adsorption, Eley-Rideal, desorption and surface rate constants in the collision theory based approach of Vincent et al.[18] and the current VTST approach.[17]

Reaction class[a]	Collision theory	Present work
Adsorption	$A = \frac{s_0}{x^x} A_{\mathrm{Pt}} N_A \Gamma \overline{v_{2\mathrm{D}}}$	$A = \frac{1}{x^x} \frac{k_B T}{h} \frac{Q_\ddagger}{Q_g}$
Eley-Rideal	$A = \frac{s_0}{x^x} A_{\mathrm{Pt}} N_A \Gamma \overline{v_{2\mathrm{D}}}$	$A = \frac{1}{x^x} \frac{k_B T}{h} \frac{Q_\ddagger}{Q_g} \frac{A_{\mathrm{B}(s)}}{A_{\mathrm{Pt}}}$
Bimolecular surface reaction Unimolecular + Pt site	$A = \frac{1}{3} \frac{2b}{x^x} N_A \Gamma^2 \overline{v_R}$	$A = \frac{1}{3} \frac{2b}{x^x} N_A \Gamma^2 \overline{v_R}$
Desorption	$A = \frac{k_B T}{h}$	$A = \frac{k_B T}{h} \frac{Q_\ddagger}{Q_s}$
Unimolecular	$A = \frac{1}{x^x} \frac{k_B T}{h}$	$A = \frac{1}{x^x} \frac{k_B T}{h}$

[a]Where x is the surface coordination of the adsorbing species, A_{Pt} and $A_{\mathrm{B}(s)}$ the projected surface areas of Pt and species B, N_A Avogadros number, b the collision radius of the reacting pair, k_B and h the Boltzmann and Planck constants and Q_X the overall partition function of species X. The velocities $\overline{v_{2\mathrm{D}}}$ and $\overline{v_R}$ correspond to the 2-dimensional Maxwellian and relative surface velocities respectively.

relies upon the UBI–QEP method for the computation of energy barriers. The robustness of the approach is assessed by formulating a second, "hybrid" mechanism where energy barriers are replaced, where possible, by the DFT based determinations of Filot et al.[40] Such a partial update is consistent with the approach of Vincent et al.[18] The applied reaction classes are shown in Table 3, where a comparison with the collision theory based approach of Vincent et al.[18] is also made. The rate parameters are naturally affected by the change from Pt to Rh. However, the overall reaction network is comprehensive and comprises 35 adsorbed species and 284 reversible reactions and should arguably not change dramatically between these metals. Hence, while all thermochemical parameters and rates of reaction were recomputed for Rh, the overall pathways were retained from the Pt surface chemistry. The ability of the resulting Rh mechanism to reproduce experimental data is explored below.

3.3.1 Pre–exponential rate parameters

The pre–exponential factors have been calculated using a systematic application of the revised class-based framework presented by Kraus and Lindstedt,[17] with the transition states

147 located using the VTST approach. The vibrational data and moments of inertia used to
148 calculate rate parameters are listed in the Supporting information.

149 3.3.2 Activation energies

150 All activation energies in the VTST rhodium mechanism were calculated using a systematic
151 application of the UBI–QEP[20] method. Values of the heats of adsorption of chemical species
152 (Q_R) were computed using this method with adjustments to the atomic heats of adsorption
153 ($Q_{\emptyset H}, Q_{\emptyset C}, Q_{\emptyset O}$) based on available literature data and sensitivity analyses (*vide infra*). The
154 total bond energies (E_R) were determined for the gas phase species and therefore retained
155 from the platinum surface chemistry.[17,18] The associated datasets are presented in Table 4.

156 A summary of the potential energy surfaces for the partial oxidation of methane over
157 rhodium has been presented by Hickman and Schmidt.[68] More recently, Filot et al.[40] investi-
158 gated syngas conversion to ethane and ethanol and provided a consistent set of high-accuracy
159 reaction energetics for hydrogenation reactions on stepped Rh surfaces. By incorporating
160 the resulting activation barriers, obtained from plane-wave calculations using the PBE-GGA
161 functional,[40] a "hybrid" mechanism is obtained. Vincent et al.[18] used the same approach to
162 provide a partial refinement of a UBI–QEP based mechanism for Pt. A comparison of se-
163 lected UBI–QEP derived activation barriers with Filot et al.[40] and Hickman and Schmidt[68]
164 is presented in Table 5. A list of all 88 pathways that were incorporated into the "hybrid"
165 mechanism is available in the Supporting information (Table S1). For some reactions the
166 UBI–QEP values are comparatively close to the values determined by Filot et al.,[40] while
167 for the CHO and CH_3O hydrogenations the discrepancies are considerable. However, the
168 UBI-QEP values are typically closer to the DFT-based values of Filot et al.[40] than the
169 suggestions by Hickman and Schmidt,[68] based on high-temperature reactor data[68] and des-
170 orption studies.[69] The potential causes of such differences and the impact on the agreement
171 with experimental data for the selected systems are discussed below.

Table 4: Heats of adsorption (Q_R) on Rh and total bond energies (E_R) for the rhodium mechanisms. Activation energies calculated using UBI–QEP,[20] unless stated otherwise.

Species	Q_R [kJ/mol]	E_R [kJ/mol]	Adsorption mode	Comment
$H(s)$	400	–	H	adjusted from 315 kJ/mol[63]
$H_2(s)$	153	431	H–H	
$O(s)$	500	–	O	calculated from O_2[64]
$O_2(s)$	235	498	–	literature[64]
$OH(s)$	259	427	O – strong	
$OOH(s)$	386	707	O – strong	
$H_2O(s)$	148	921	O	
$H_2O_2(s)_2$	154	1071	OH–OH	
$C(s)_3$	583	–	C	$Q_{\emptyset C}$ = 350 kJ/mol
$CH(s)_3$	285	339	C – medium	
$CH_2(s)_2$	162	762	C – medium	
$CH_3(s)$	77	1227	C – medium	$Q_{\emptyset C}$ = 222 kJ/mol[65]
$CCH(s)$	103	1084	C – medium	$Q_{\emptyset C}$ = 350 kJ/mol
$CCH_2(s)_2$	199	1457	C – medium	
$CCH_2(s)_3$	505	1457	C=CH_2 + π	
$CCH_3(s)_3$	252	1569	C – medium	
$CHCH_2(s)$	85	1787	C – medium	
$CHCH_2(s)_3$	87	1787	CH–CH_2	
$CHCH_3(s)_2$	170	1934	C – medium	
$CH_2CH_3(s)$	79	2412	C – medium	
$C_2H_2(s)_3$	31	1641	CH=CH + π	
$C_2H_4(s)$	8	2252	CH_2=CH_2 + π	
$C_2H_4(s)_2$	15	2252	CH_2–CH_2 (di-σ)	
$C_2H_6(s)_2$	8	2822	CH_3–CH_3	
$CO(s)_2$	166	1076	C – medium	literature[66]
$CO_2(s)_2$	72	1608	–	literature[67]
$CHO(s)$	84	1147	C – medium	$Q_{\emptyset C}$ = 350 kJ/mol
$COH(s)_3$	269	965	C – medium	
$CHOH(s)_2$	90	1300	C – medium	
$COOH(s)$	79	1646	C – strong	
$CH_2O(s)$	104	1511	O	
$CH_2OH(s)$	303	1637	C – medium	$Q_{\emptyset C}$ = 350 kJ/mol
$CH_3O(s)$	291	1603	O – strong	
$CH_3OH(s)$	189	2039	O	
CH_4	25	1666	–	literature[65]
C_2	71	609	C≡C	$Q_{\emptyset C}$ = 350 kJ/mol

Table 5: Comparison of activation barriers of selected reactions: Oxidation of C to CO_2, hydrogenation of CHO to CH_3OH, methyl recombination, H/O submechanism. Barrier heights in [kJ/mol].

Reaction	Filot et al.[40]	UBI–QEP	Hickman and Schmidt[68]
$C(s)_3 + O(s) \rightarrow CO(s)_2 + 2(s)$	92	63	60
$CO(s)_2 + O(s) \rightarrow CO_2(s)_2 + (s)$	80	79	105
$CHO(s) + H(s) \rightarrow CH_2O(s) + (s)$	69	0	–
$CH_3O(s) + H(s) \rightarrow CH_3OH(s) + (s)$	60	96	–
$CH_3(s) + H(s) \rightarrow CH_4 + 2(s)$	36	20	–
$O(s) + H_2O(s) \rightarrow OH(s) + OH(s)$	53	155	265
$OH(s) + OH(s) \rightarrow O(s) + H_2O(s)$	53	0	63
$H(s) + O(s) \rightarrow OH(s) + (s)$	156	184	84
$OH(s) + (s) \rightarrow H(s) + O(s)$	142	5	21
$H(s) + OH(s) \rightarrow H_2O(s) + (s)$	108	60	34
$H_2O(s) + (s) \rightarrow H(s) + OH(s)$	77	85	155

3.3.3 Comments on heats of adsorption

To obtain accurate data on atomic heats of adsorption presents a significant challenge. Considerable discrepancies between experimental and computational studies are not uncommon and, furthermore, values often have to be back-calculated from related experimental data. For example, the experimental investigation into oxygen interactions with rhodium surfaces by Thiel et al.[64] suggested a barrier to oxygen desorption of 235 kJ/mol. The calorimetric study of Wang et al.[70] reported a consistent value of the heat of adsorption of 296 kJ/mol for molecular oxygen. However, Inderwildi et al.[71] investigated O and O_2 adsorption on rhodium using PW91-GGA DFT and reported a low-coverage value of $Q_{O_2} = 96$ kJ/mol. The latter DFT result appears inconsistent with data on other metals such as palladium[20,72] and iridium.[73] The heat of adsorption of O_2 was therefore set to the experimental value of 235 kJ/mol[64] and the corresponding atomic heat of adsorption $Q_{\emptyset O}$ of 500 kJ/mol was obtained via UBI–QEP. The applied value of $Q_O = 500$ kJ/mol was also calculated using UBI–QEP assuming adsorption on the on-top site; the more common assumption of adsorption into a threefold hollow site would lead to an arguably unreasonably high value of 833 kJ/mol. The value for OH was set to the UBI–QEP derived value of 259 kJ/mol. The stability of OH in catalytic reforming of methane has been identified as a sensitive parameter for selectivity to H_2.[14] The activation barriers for the decomposition of OH(s), shown in Table 5, vary considerably. The UBI–QEP method predicts a low barrier, due to the exothermic nature of the process, while the slightly higher value used by Hickman and Schmidt[68] was obtained from OH desorption and hydrogen oxidation data.[69] The much higher value obtained by Filot et al.[40] is consistent with an early transition state where the dissociation of the O–H bond (427 kJ/mol) plays a significant role.

Literature data for adsorption of carbon species on rhodium is available for CH_4[65] and for C_6-C_{10} compounds.[74] A study of carbon interactions with Rh surfaces reports a binding energy of edge carbon atoms as 222 kJ/mol.[75] The resulting UBI–QEP value of $Q_{CH_4} = 25$ kJ/mol is consistent with the experimental data of Brass and Ehrlich.[65] How-

ever, a systematic application of $Q_{\emptyset C} = 222$ kJ/mol leads to very low heats of adsorption for most other carbon–bound compounds with, for example, $Q_{C_2H_4}$ and $Q_{C_2H_6}$ below 2 kJ/mol. Accordingly, heats of adsorption of most carbon–bound species were calculated using an adjusted value of $Q_{\emptyset C} = 350$ kJ/mol, which provides good agreement with the experimental value for CO. The lower value of 222 kJ/mol[75] was retained only for CH_3 and CH_4.

Adsorption of CO is comparatively well studied. Experimental determinations by Baraldi et al.,[76] Dulaurent et al.[77] and Smedh et al.[78] estimate a barrier to desorption of around 140 kJ/mol. The value depends on the coverage[78] and the geometry of the adsorbed species.[77] A higher initial value of 160 kJ/mol at very low coverages was proposed by He et al.[79] The latter is supported by the experimental study by Jansen et al.[66] that reports a heat of adsorption of 160 kJ/mol and barrier to desorption of 132 kJ/mol. An UBI–QEP calculation using $Q_{\emptyset C} = 350$ kJ/mol produces a consistent value of $Q_{CO} = 166$ kJ/mol. The heat of adsorption of CO_2 has been determined using PW91-GGA DFT by Chang and Ho[67] on various Rh clusters and an intermediate value of 72 kJ/mol was chosen from the reported range of 68–85 kJ/mol.

Rojo et al.[63] studied molecular hydrogen adsorption experimentally and proposed a value of 40 kJ/mol. The value is consistent with the suggestion by Savargaonkar et al.[80] that "the heat of adsorption of hydrogen on rhodium is about 13 kJ/mol higher than that on platinum". A combination with the value for Pt suggested by Vincent et al.[18] also yields $Q_{H_2} = 40$ kJ/mol for Rh. However, use of the corresponding UBI–QEP derived $Q_H = 315$ kJ/mol leads to overall poor agreement with a sensitivity analysis targeting Q_H and Q_{H_2} suggesting an increase to $Q_H = Q_{\emptyset H} = 400$ kJ/mol. Given the large adjustment, results are shown below for both the VTST-based mechanism and the "hybrid" alternative featuring the hydrogenation energy barriers of Filot et al.[40]

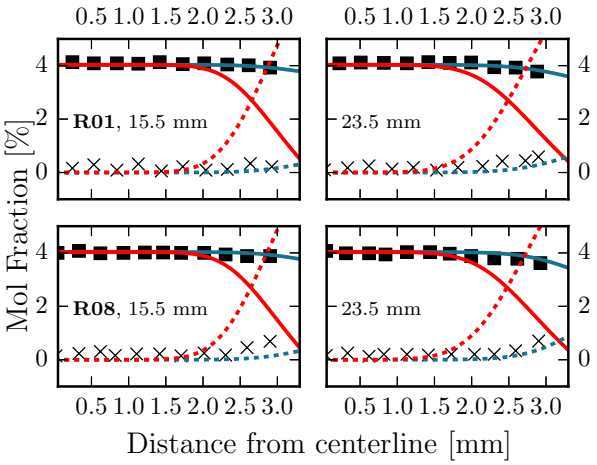

Figure 2: Experimental (symbols) and computational (lines) transverse mol fraction profiles for cases **R01** and **R08** of Reinke et al.:[42] CH_4 (■, ——) and H_2O (×, - - - -). Calculations performed with the following surface/gas mechanisms: VTST/L+S[17,56] (—) and Vincent et al./L+S[18,56] (—).

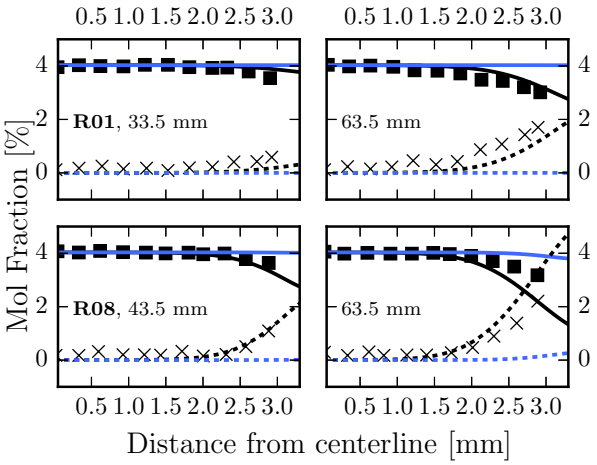

Figure 3: Experimental and computational transverse mol fraction profiles for cases **R01** and **R08** of Reinke et al.[42] at further downstream locations. Symbols as in Fig. 2. Calculations performed with the following surface/gas mechanisms: VTST/L+W[17,55] (—) and L+W only[55] (—).

4 Results and discussion

4.1 Fuel-lean combustion of methane over Pt

The results obtained for fuel-lean combustion of methane over Pt using the VTST mechanism of Kraus and Lindstedt[17] are shown in Figs. 2 and 3 for cases **R01** and **R08** at $\phi = 0.40$, and in Figs. 4 and Fig. 5 for cases **R06**, **R13** and **R15** at $\phi = 0.35$. The mechanism provides agreement within 1 mol% for the experimental data of Reinke et al.[42] Furthermore, the effects of pressure are correctly reproduced for the range of 4 to 16 bar. As shown in Fig. 3, the conversion of methane is seriously under–predicted in the absence of surface chemistry.

The results obtained with the mechanism of Vincent et al.,[18] coupled with the gas phase chemistry of Lindstedt and Skevis,[56] are shown in Figs. 2 and 4. The conversion of methane is over–predicted for all cases. The VTST mechanism coupled to the same gas phase chemistry predicts conversion at the first two sampling points correctly. The impact of the updated gas phase chemistry is discussed further below.

4.2 Catalytic partial oxidation of methane over Pt

The results for catalytic partial oxidation of methane over Pt, obtained using the VTST mechanism of Kraus and Lindstedt[17] are shown in Figs. 6 and 7 for case **Pt1** and in Fig. 8 for case **Pt3**. The predicted mol fraction profiles of CH_4 and O_2 show agreement with experimental data to within 2 mol% at all downstream locations. The CO production is under-predicted by 1 mol% in the first part of the reactor, as shown in Fig. 6. However, the agreement improves beyond 50 mm downstream. The H_2 mol fraction is over-predicted by up to 1 mol% for case **Pt1** at all downstream distances, especially close to the catalytic surface. The agreement is better for higher stoichiometries (ϕ) as shown in Fig. 8.

The results obtained with the mechanism of Vincent et al.[18] are shown for case **Pt1** in Figs. 6 and 7. The mol fraction profiles of CH_4, H_2 and O_2 are in better agreement

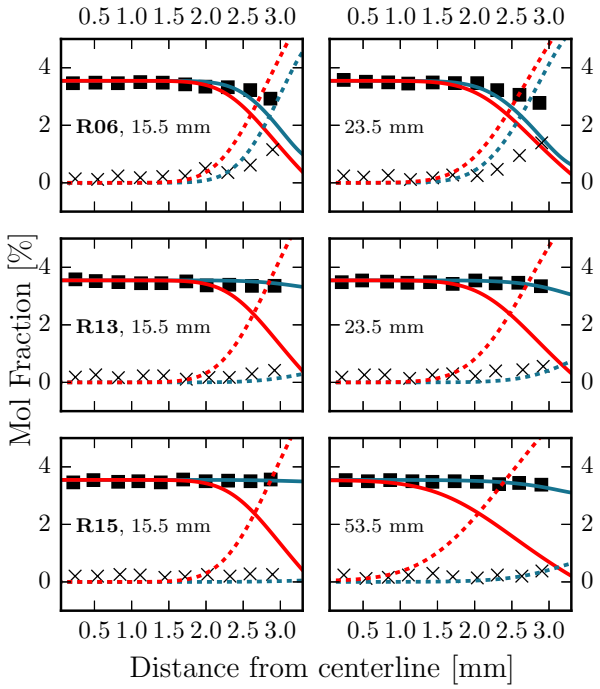

Figure 4: Experimental (symbols) and computational (lines) transverse mol fraction profiles for cases **R06**, **R13** and **R15** of Reinke et al.:[42] CH_4 (■, ——) and H_2O (×, - - - -). Calculations performed with the following surface/gas mechanisms: VTST/L+S[17,56] (—) and Vincent et al./L+S[18,56] (—).

with experiment as compared to the results obtained with the VTST mechanism. However, the agreement for CO is poor beyond 51 mm downstream, where the mechanism fails to capture the production of CO close to the catalytic surface. The difference between the two mechanisms is mainly caused by the different O adsorption rates as discussed by Kraus and Lindstedt.[17] With the VTST mechanism, the O(s) coverage in the first few mm of the reactor approaches 40%. The onset of CO production coincides with the depletion of surface O(s) that occurs around 35 mm downstream. By comparison, the surface coverage of O(s) is insignificant throughout the reactor when the mechanism of Vincent et al.[18] is applied. The discrepancy is consistent with the application of the experimental sticking coefficient for O_2 dissociative adsorption[26,81] and the associated treatment of related oxygen adsorption processes.[17]

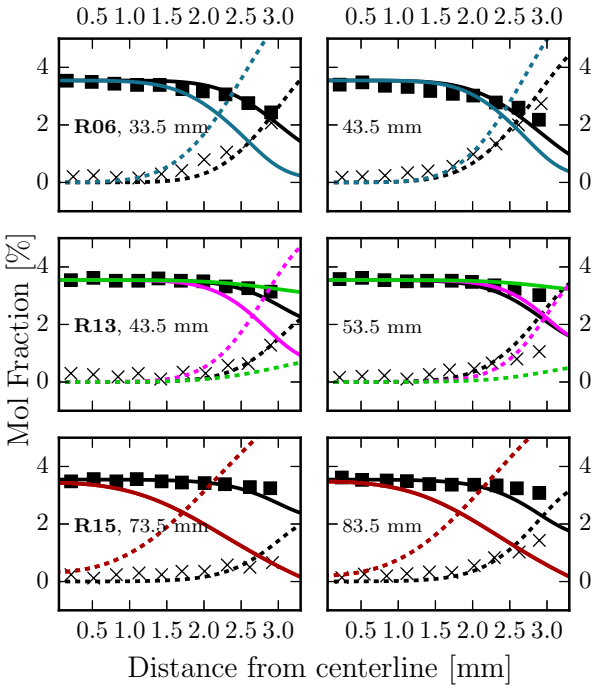

Figure 5: Experimental and computational transverse mol fraction profiles for cases **R06**, **R13** and **R15** of Reinke et al.[42] at further downstream locations. Symbols as in Fig. 4. Calculations performed with the following surface/gas mechanisms: VTST/L+S[17,56] (—) and VTST/L+W[17,55] (—); VTST/L+W with an adjusted methane oxidation rate (4) of Quiceno et al.:[59] (×8 —, $\times\frac{1}{8}$ —); and Vincent et al./L+W[18,55] (—).

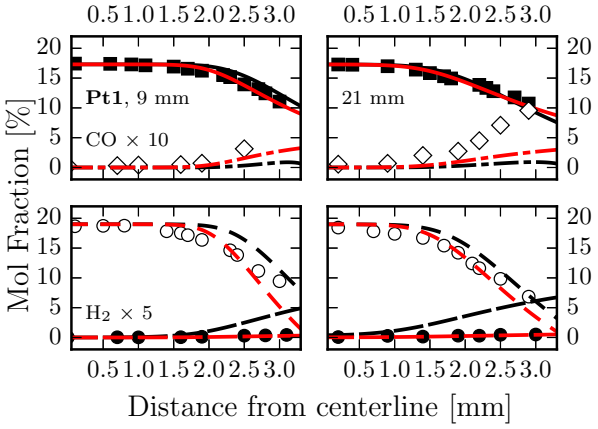

Figure 6: Experimental (symbols) and computational (lines) transverse mol fraction profiles for case **Pt1** of Sui et al.:[45] CH_4 (■, ——), CO (◇, — -, ×10), O_2 (○, - - -) and H_2 (•, — —, ×5). Calculations performed with the following surface/gas mechanisms: VTST/L+W[17,55] (—) and Vincent et al./L+S[18,56] (—).

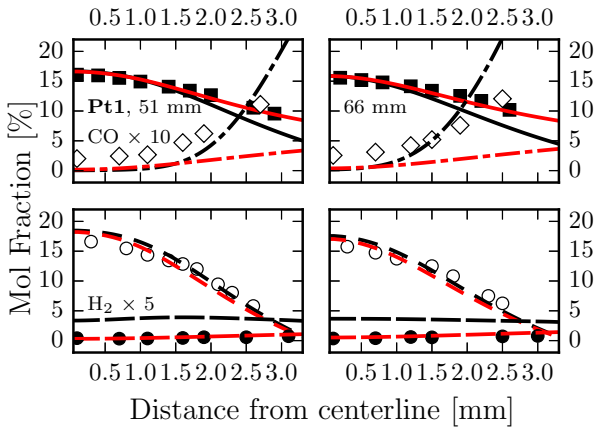

Figure 7: Experimental and computational transverse mol fraction profiles for case **Pt1** of Sui et al.[45] at further downstream distances. Symbols and lines as in Fig. 6.

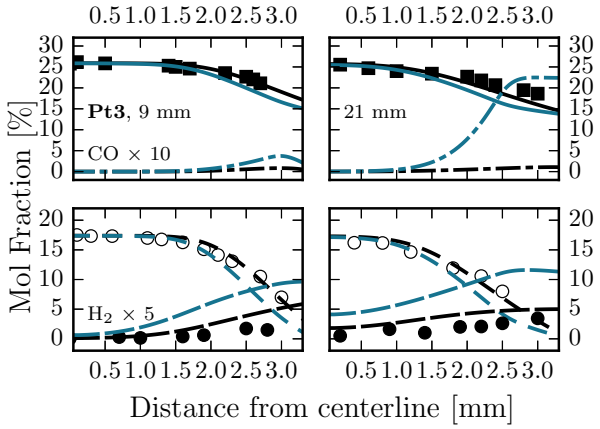

Figure 8: Experimental (symbols) and computational (lines) transverse mol fraction profiles for case **Pt3** of Sui et al.[45] Symbols as in Fig. 6. Calculations performed with the following surface/gas mechanisms: VTST/L+S[17,56] (—) and VTST/L+W[17,55] (—).

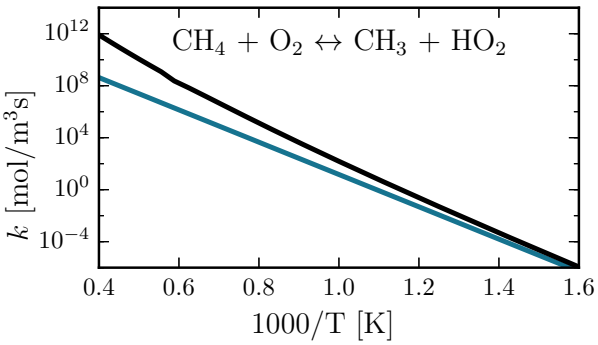

Figure 9: Arrhenius plot of the rate of reaction (4). The rate used by Lindstedt and Skevis[56] was proposed by Baulch et al.[57] (—) and that used by Lindstedt and Waldheim[55] by Quiceno et al.[59] (—). The latter was calculated from the reverse rate and the equilibrium constant.

4.3 Impact of gas phase chemistry

As shown in Figs. 5 and 8, results obtained with the updated gas phase chemistry of Lindstedt and Waldheim[55] (L+W) differ considerably from the results with gas phase chemistry of Lindstedt and Skevis[56] (L+S). The effect on the conversion of methane beyond 30 mm downstream, shown in Fig. 5, is particularly pronounced. Another effect is the peak in the CO mol fraction away from the catalytic wall, shown in Fig. 8. The cause is the updated rates for some of the CH_3 pathways in the mechanism of Lindstedt and Waldheim:[55]

$$CH_3 + CH_3 \rightleftharpoons C_2H_5 + H \tag{1}$$

$$CH_3 + CH_3 + (M) \rightleftharpoons C_2H_6 + (M) \tag{2}$$

$$CH_3 + O_3 \rightleftharpoons CH_2O + OH \tag{3}$$

$$CH_4 + O_2 \rightleftharpoons CH_3 + HO_2 \tag{4}$$

Reaction (4) is the most sensitive. A comparison of the alternative rates of reaction[55,56] is shown in Fig. 9. For temperatures above 1000 K, the rate proposed by Quiceno et al.[59] is considerably faster than the recommendation by Baulch et al.[57] The sensitivity analysis for reaction (4), shown in Fig. 5, confirms that an increase of the rate (×8) results in lower

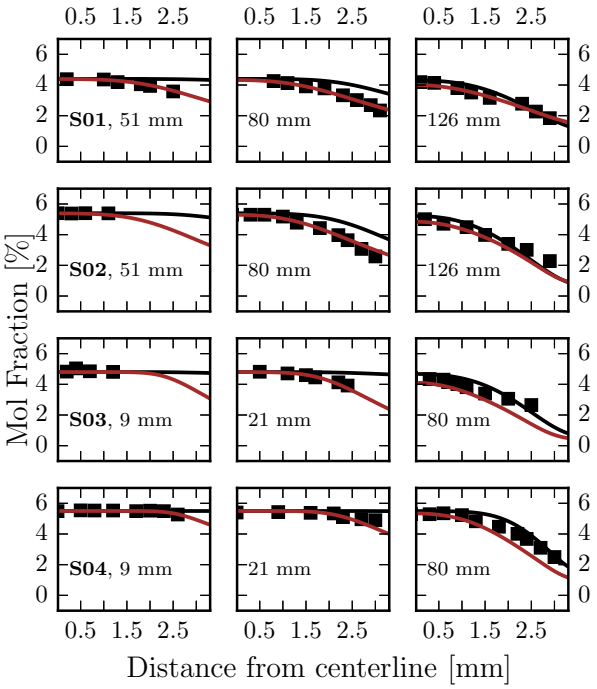

Figure 10: Experimental (■) and computational (——) transverse mol fraction profiles of CH_4 for fuel-lean cases **S01**–**S04** of Sui et al.[44] Calculations performed with gas phase chemistry of Lindstedt and Waldheim[55] coupled to the VTST mechanism for Rh (**—**), and the "hybrid" mechanism for Rh (**—**).

conversion of CH_4. This can be explained by interactions with the surface chemistry. The CH_3 radicals produced by the catalytic surface are converted back to CH_4 via the reverse of this pathway. The surface chemistry of Vincent et al.[18] over–predicts CH_4 conversion even when coupled to the gas phase chemistry of Lindstedt and Waldheim[55] (*cf.* Fig. 5).

4.4 Fuel-lean combustion of methane over Rh

The results for cases **S01**–**S04** investigated by Sui et al.[44] for fuel-lean combustion of methane over rhodium are presented in Fig. 10. The VTST mechanism under-predicts conversion by up to 1.5 mol% in the first 80 mm of the reactor for cases **S01** and **S02** and to a lesser extent for cases **S03** and **S04**. The "hybrid" mechanism, augmented with activation barriers of Filot et al.,[40] shows improved agreement with experimental CH_4 profiles due to the increased barrier to methyl recombination with $H(s)$ via reaction (5).

$$\mathrm{CH_3}(s) + \mathrm{H}(s) \rightarrow \mathrm{CH_4} + 2(s) \left\langle \begin{array}{l} 20 \text{ kJ/mol, UBI–QEP}^{20} \\ 36 \text{ kJ/mol, Filot et al.}^{40} \end{array} \right. \quad (5)$$

A surface site coverage analysis shows that in the first 50 mm of the reactor $\theta_{\mathrm{CH_3}}$ is up to three orders of magnitude higher with the "hybrid" mechanism. For both mechanisms $\mathrm{O}(s)$ and $\mathrm{H}(s)$ are dominant surface species with coverages $\theta_{\mathrm{O}(s)} > 70\%$ and $\theta_{\mathrm{H}(s)} > 1\%$. As a consequence, the rate of reaction (5) is effectively zero-order in $\mathrm{H}(s)$ and first order in $\mathrm{CH_3}(s)$. For the cases at 5 bar (**S03** and **S04**) gas phase ignition is predicted to occur around 110 mm downstream with both mechanisms. Therefore the data obtained for the sampling point at 126 mm are not shown. Results obtained with the VTST mechanism coupled to the gas phase scheme of Lindstedt and Skevis[56] predict an ignition distance around 80 mm.

4.5 Catalytic partial oxidation of methane over Rh

Results of partial catalytic oxidation of methane over rhodium for case **A01** (4 bar, $\phi = 4$) are presented at four downstream locations in Figs. 11 and 12. The VTST mechanism predicts $\mathrm{CH_4}$ and $\mathrm{O_2}$ conversion within 1 mol% in the first 52 mm of the reactor. Major products ($\mathrm{H_2}$, $\mathrm{H_2O}$ and $\mathrm{CO_2}$) are reproduced with similar accuracy with the exception of CO, which is under-predicted by up to 4 mol% close to the catalytic surface. The agreement with experimental data decreases further downstream, as shown in Fig. 12, due to accumulation of discrepancies. Selectivities towards CO and $\mathrm{H_2}$ are under-predicted by up to 6 mol% as a consequence of the slower conversion of $\mathrm{CH_4}$ at the catalytic surface. Application of the higher value of $\mathrm{Q}_{\emptyset\mathrm{C}} = 350$ kJ/mol for $\mathrm{CH_3}$ and $\mathrm{CH_4}$ does not lead to increased conversion and it is evident that uncertainties remain. The "hybrid" mechanism shows comparable behaviour in the first part of the reactor. However, further downstream the "hybrid" mechanism is more selective to $\mathrm{H_2O}$ leading to a further under-prediction of $\mathrm{H_2}$ as a direct consequence of the updated barriers shown in Table 5.

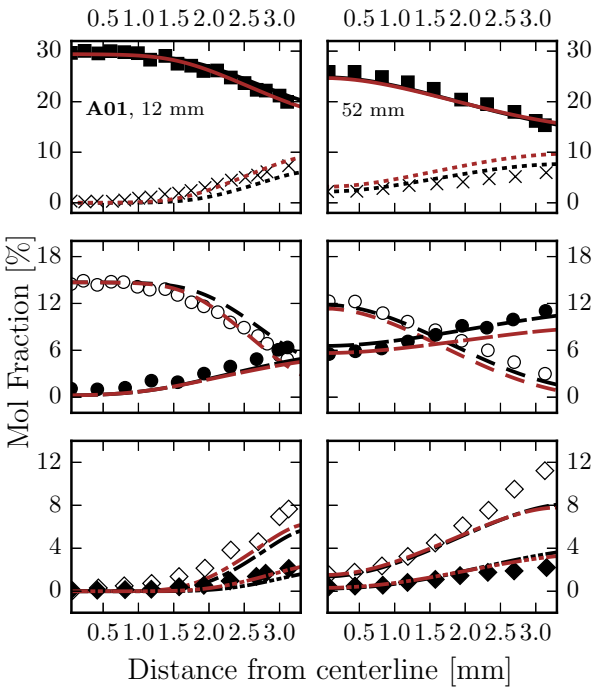

Figure 11: Experimental (symbols) and computational (lines) transverse mol fraction profiles for partial oxidation case **A01** of Appel et al.:[43] CH_4 (■,——), H_2O (×,- - - -), O_2 (○, - - -), H_2 (●, — —), CO (◇,— -) and CO_2 (◆, —···). Calculations performed with the VTST mechanism for Rh (**—**), and the "hybrid" mechanism for Rh (—).

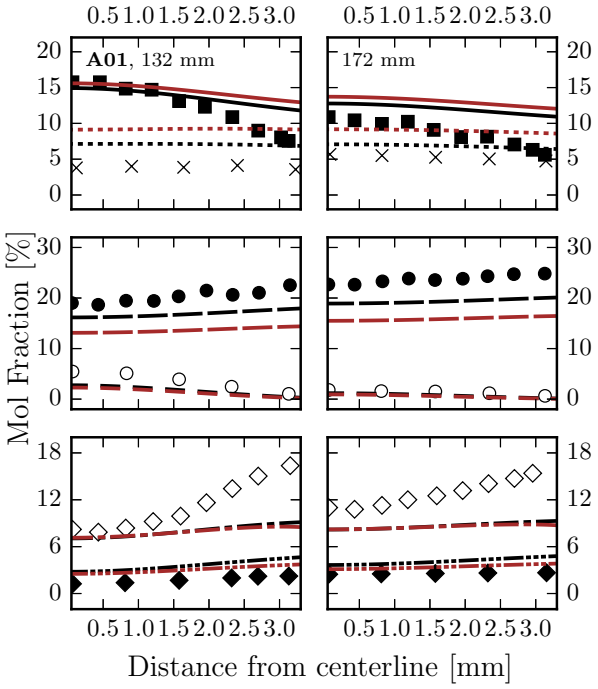

Figure 12: Experimental and computational transverse mol fraction profiles for partial oxidation case **A01** of Appel et al.[43] at further downstream distances. Symbols and lines as in Fig. 11.

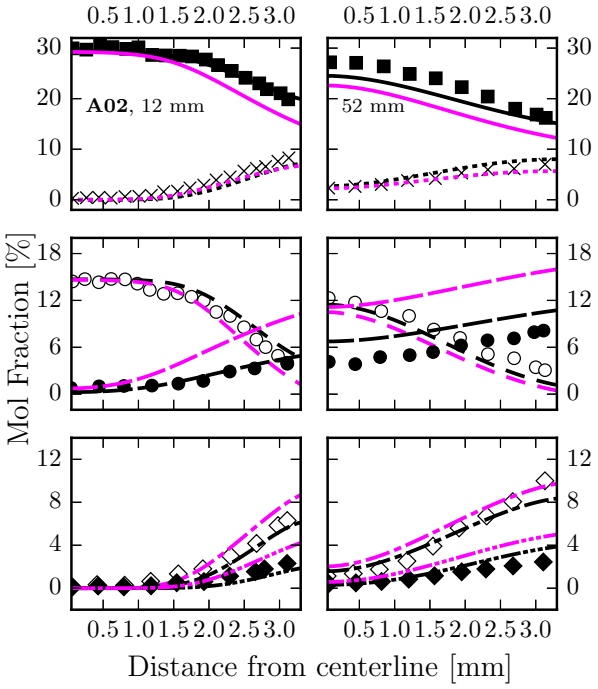

Figure 13: Experimental and computational transverse mol fraction profiles for partial oxidation case **A02** of Appel et al.[43] Symbols as in Fig. 11. Calculations performed with the VTST mechanism for Rh (—) and with a 10% decrease in Q_{H_2} and Q_H (—).

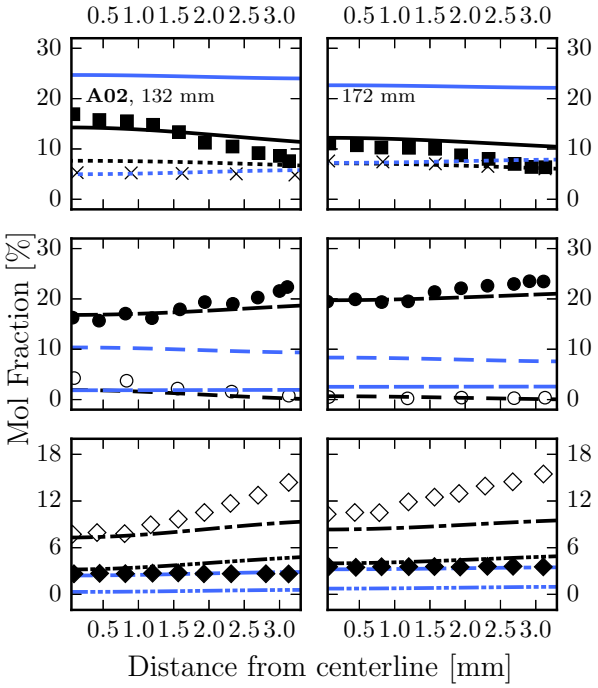

Figure 14: Experimental and computational transverse mol fraction profiles for partial oxidation case **A02** of Appel et al.[43] at further downstream distances. Symbols as in Fig. 11. Calculations performed with the VTST mechanism for Rh (—) and with gas phase chemistry of Lindstedt and Waldheim[55] only (—).

The results for case **A02** at 6 bar are presented in Figs. 13 and 14. The mol fraction profiles obtained with the VTST mechanism are consistent with case **A01**. However, the agreement for H_2 and CH_4 in the latter parts of the reactor (see Fig. 14) is improved. The largest discrepancy with experimental data is for the CO close to the catalytic surface with an under-prediction of 6.5 mol% as a result of the lower CH_4 conversion. The sensitivity of the VTST mechanism to the values of Q_{H_2} and Q_H is shown in Fig. 13. An increase of 10% causes a complete loss of conversion, while a decrease by 10% doubles H_2 production and increases CH_4 conversion in the first part of the reactor. This sensitivity towards the energetics of H and H_2 is further supported by the results obtained with the "hybrid" mechanism (see Figs. 11 and 12), where the energetics of the hydrogenation reactions were obtained from the DFT study by Filot et al.[40] as shown in Table 5 (the full list of 88 updated barriers is available in the Supporting information). The H_2/O_2 surface chemistry is particularly affected by small changes in Q_H and is coupled to CH_4 conversion via surface reaction (5) and gas phase reaction (4). It is shown in Fig. 14 that the overall conversion and the selectivity towards syngas is dependent on the contribution of surface chemistry. Computations with only gas phase chemistry show a considerably reduced conversion with complete combustion products (CO_2 and H_2O) favoured over syngas (CO and H_2). Hence, while the gas phase chemistry is important in the current systems, the major trends are determined by the catalyst.

For case **A03**, including gas phase ignition, the computational results follow the same general trends as for the previous two cases and are therefore not shown. The VTST mechanism provides agreement to within 1 mol% of the experimental data for all studied species at 12 and 52 mm downstream. Figure 15 shows a map of OH mol fraction and a contour plot of temperature for this case, computed with the gas phase mechanism of Lindstedt and Waldheim.[55] Experimentally measured ignition points are between 72–92 mm downstream[43] with the current computations showing a slightly delayed onset at just below 100 mm. However, the over-prediction is consistent with calculations of Appel et al.[43] using the gas phase model of Warnatz et al.[82] Calculations using the gas phase mechanism of Lindstedt and

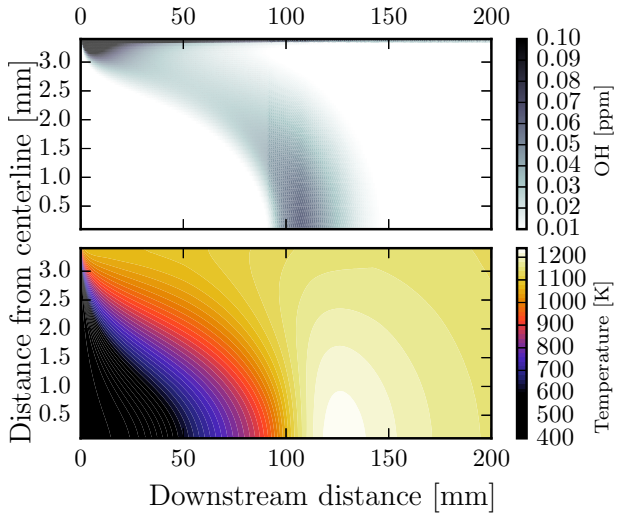

Figure 15: A map of OH mol fraction (top) and a contour plot of temperature (bottom) for case C03. Calculated using the VTST mechanism for Rh with the gas phase chemistry of Lindstedt and Waldheim.[55]

Skevis[56] result in a large under-prediction of the ignition distance ($<$ 30 mm downstream) and uncertainties in the gas phase chemistry are hence a major cause of discrepancies.

The results for partial oxidation over Rh for case **Rh1** of Sui et al.[45] are shown in Figs. 16 and 17. The VTST mechanism provides good agreement with the experimental CH_4 and O_2 mol fraction profiles. The slightly over-predicted CH_4 conversion results in an over-prediction in H_2 and CO mol fractions by up to 4 and 3 mol% respectively. The results obtained with the "hybrid" mechanism are comparable with the exception of H_2 where the agreement is improved to within 2 mol%, as a consequence of the updated energy barriers[40] in the hybrid mechanism. The mol fraction profiles predicted by the two mechanisms for case **Rh3**[45] are shown in Fig. 18. The trends are consistent with the previously observed behaviour – the VTST mechanism over-estimates H_2 production by up to 6 mol% at the location 66 mm downstream, while the "hybrid" mechanism is more selective towards H_2O, resulting in a better agreement in the H_2 profile. The hybrid mechanism contains increased forward barriers for reactions leading to H_2O formation, which would suggest a decrease in selectivity. However, the barrier in the dissociation of OH(s) to H(s) and O(s) has been updated from 5 kJ/mol (UBI–QEP) to 142 kJ/mol (Filot et al.[40]), accompanied by a

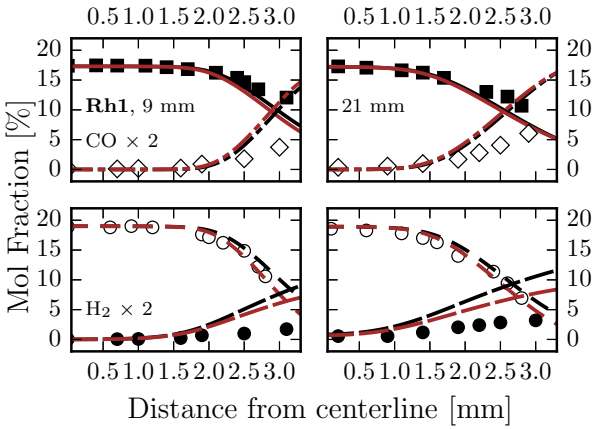

Figure 16: Experimental (symbols) and computational (lines) transverse mol fraction profiles for partial oxidation case **Rh1** of Sui et al.:[45] CH_4 (■, ——), CO (⋄, — -, ×2), O_2 (○, - - -), H_2 (•, — —, ×2). Calculations performed with the VTST mechanism for Rh (**—**) and with the "hybrid" mechanism for Rh (—).

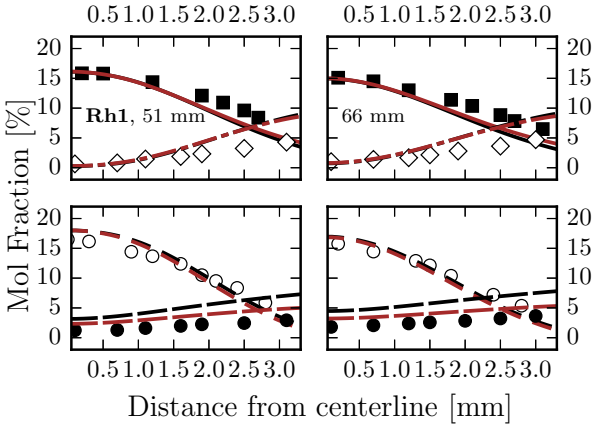

Figure 17: Experimental and computational transverse mol fraction profiles for partial oxidation case **Rh1** of Sui et al.[45] at further downstream distances: CH_4 (■, ——), CO (⋄, — -), O_2 (○, - - -), H_2 (•, — —). Calculations performed with the VTST mechanism for Rh (**—**) and with the "hybrid" mechanism for Rh (—).

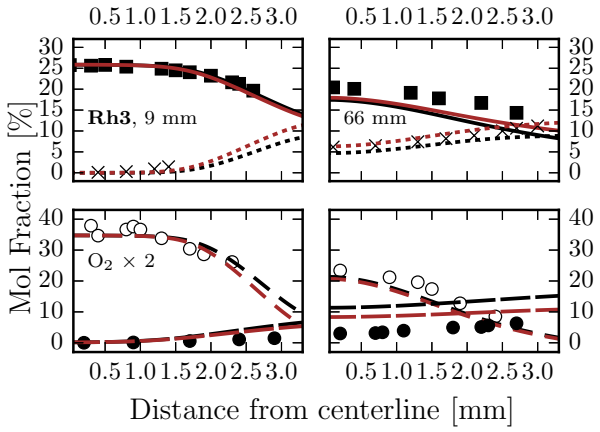

Figure 18: Experimental (symbols) and computational (lines) transverse mol fraction profiles for partial oxidation case **Rh3** of Sui et al.:[45] CH_4 (■, ——), H_2O (×, - - - -), O_2 (○, - - -, ×2), H_2 (•, — —). Calculations performed with the VTST mechanism for Rh (—) and with the "hybrid" mechanism for Rh (—).

decrease in the barrier for the reverse reaction leading to an increase of OH on the surface. Enger et al.[14] highlighted the importance of the stability of OH for the selectivity to H_2 and the current results support this conclusion.

Given the uncertainties associated with the atomic heat of adsorption of hydrogen ($Q_{\emptyset H}$) and the potential impact on OH formation on the surface, a sensitivity analysis was performed for case **Rh3** using the hybrid mechanism that incorporates the energy barriers of Filot et al.[40] A decrease in $Q_{\emptyset H}$ of just 5% (*i.e.* with $Q_{\emptyset H}$ = 385 kJ/mol) causes a complete loss of conversion. The resulting surface site coverages for this case are shown in the two panels on the left of Fig. 19. For values of $Q_{\emptyset H}$ below 385 kJ/mol the surface becomes covered in $CH(s)_3$ and $COOH(s)$ as shown in Fig. 19(a). The use of $Q_{\emptyset H}$ = 400 kJ/mol results in approximately 50% free sites with a wide range of other adsorbates as shown in Fig. 19(b). This implies a strong coupling between $Q_{\emptyset H}$ and the heat of adsorption of $CH(s)_3$ and $COOH(s)$. A similar analysis was performed for case **A02** using the VTST mechanism as shown in the two panels on the right of Fig. 19. Again, with $Q_{\emptyset H}$ = 400 kJ/mol (*cf.* Fig. 19(c)) the total surface coverage remains below unity allowing reactions to proceed. For values $Q_{\emptyset H} > 440$ kJ/mol (*cf.* Fig. 19(d)) the surface beomes completely covered, predominantly by $H(s)$. The above analysis suggests that $Q_{\emptyset H} \simeq 400$ kJ/mol is compatible with

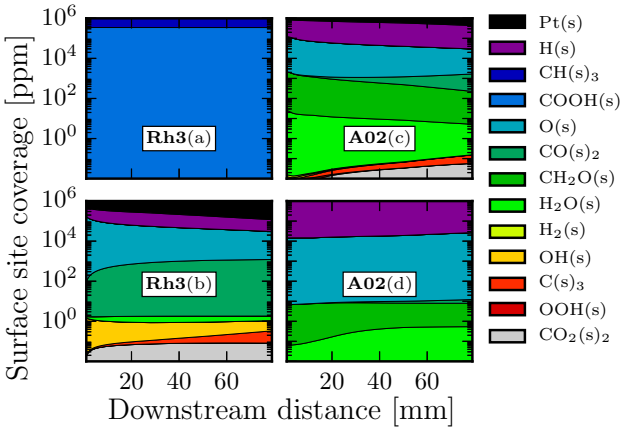

Figure 19: Surface site coverage analysis for partial oxidation over Rh. Case **Rh3** (left), calculated with the "hybrid" mechanism, $Q_{\emptyset H}$ of 380 kJ/mol (a) and 400 kJ/mol (b). Case **A02** (right), calculated with the VTST mechanism, $Q_{\emptyset H}$ of 400 kJ/mol (c) and 440 kJ/mol (d).

both the direct application of the UBI-QEP method as well as when combined with the more accurate energy barriers determined by Filot et al.[40]

5 Conclusions

An extended suite of test data, including methane conversion over Pt under fuel-lean combustion[42] and partial oxidation[45] conditions, supplements our previous work (*c.f.* Kraus and Lindstedt[16,17]). It has been shown that the systematic application[17] of VTST combined with UBI–QEP[20] for the determination of energy barriers can equal or surpass the agreement obtained with the corresponding models derived on the basis of sticking coefficients.[18] The VTST approach accordingly appears a promising route leading to the potential elimination of the difficulties associated with the scarcity of such data. It has further been shown that the contribution of the gas phase chemistry, while secondary in key aspects, remains significant: a sensitivity analysis has shown that the rate of $CH_4 + O_2 \leftrightharpoons CH_3 + HO_2$ is the most sensitive parameter under the current conditions due to a strong coupling with the heterogeneous chemistry. It has also been shown that the faster rate suggested by Quiceno et al.[59] provides better agreement than the recommendation of the CEC data evaluation group.[57] The combined updated mechanism produces quantitative agreement with the experimental

data within 1 mol% at all pressures and downstream distances.

To provide a further evaluation of the feasibility of the method, a reaction mechanism for Rh was developed using the same systematic approach, with its accuracy assessed under similar conditions[43–45] to those used for Pt in the current study. The heats of adsorption were obtained from literature and were subject to sensitivity analysis. It was shown that for some species (e.g. H and H_2) significant uncertainties remain. Accordingly, data on energy barriers from DFT studies of the CH_4/syngas system on Rh[40,68] were incorporated to provide a partially updated "hybrid" mechanism following the approach of Vincent et al.[18] For fuel-lean mixtures, the derived VTST mechanism under-predicts CH_4 conversion by up to 1.5 mol% in the early part of the reactor, while the "hybrid" mechanism reproduces the experimental mol fraction profiles well within 1 mol%, as a consequence of an updated barrier for methyl recombination. Under CPO conditions, the VTST mechanism shows good agreement below 52 mm downstream and is generally within 2 mol% of the experimental data. The exception is for CO at downstream distances beyond 130 mm where an under-prediction up to 6 mol% is obtained close to the catalytic surface. Possible explanations include (i) an accumulation of discrepancies in the early part of the reactor and (ii) the uncertainties in heats of adsorption of $Q_{\emptyset H}$ and $Q_{\emptyset C}$. Additionally, the application of the UBI–QEP method for CO adsorption is arguably beyond the scope of the method.[20] The agreement with experimental data can accordingly be further improved by incorporating higher-accuracy determinations of barrier heights.[40] However, the proposed framework appears robust and appropriate the for rapid development of surface mechanisms while also serving as basis for the progressive inclusion of more accurate data for sensitive pathways such as $CH_3(s)$+$H(s)$ recombination.

Supporting information

The files *chem.txt*, *tran.txt* and *therm.txt* include the fully referenced gas phase mechanism of Lindstedt and Waldheim[55] as applied, including thermochemistry and transport data,

in Chemkin-II format. The files *Rh-VTST.txt* and *Rh-hybrid.txt* contain the heterogeneous VTST and "hybrid" mechanism for Rh, including thermochemistry. The file *Rh-35+5+4.txt* contains species' data used to create the VTST mechanism for Rh, including the vibrational frequencies, moments of inertia, and heats of adsorption, in a JSON format. All of the above are in a machine-readable format. The file *SI.pdf* contains the list of the 88 barrier heights of Filot et al.[40] incorporated into the "hybrid" mechanism (Table S1).

Acknowledgements

R. P. Lindstedt and P. Kraus would like to thank Dr. I. Sakata and Dr. K. Gkagkas of Toyota Motor Europe for supporting this work and Dr. J. Mantzaras of Paul Scherrer Institute for sharing his experimental data and associated discussions.

References

(1) van der Laan, G. P.; Beenackers, A. A. C. M. Kinetics and selectivity of the Fischer-Tropsch synthesis: A literature review. *Catal. Rev. Sci. Eng.* **1999**, *41*, 255–318.

(2) Fong, W.-C. F.; Wilson, R. F. Gasification process combined with steam methane reforming to produce syngas suitable for methanol production. US patent no. US5496859, 1995.

(3) Wang, Z. *Compr. Org. Name React. Reagents*; 2010; pp 2454–2457.

(4) Crabtree, G. W.; Dresselhaus, M. S.; Buchanan, M. V. The hydrogen economy. *Phys. Today* **2004**, *57*, 39–44.

(5) Sabatier, P. The Nobel Prize in Chemistry 1912. 1912; `http://www.nobelprize.org/nobel_prizes/chemistry/laureates/1912/`.

(6) Liquid methane fuel characterization and safety assessment report. 1991; http://www.cryogenicfuelsinc.com/includes/LiquidMethaneSafetyReport.pdf.

(7) UnionGas, Chemical composition of natural gas. 2016; https://www.uniongas.com/about-us/about-natural-gas/Chemical-Composition-of-Natural-Gas.

(8) Tong, X.; Smith, L. H.; McCarty, P. L. Methane fermentation of selected lignocellulosic materials. *Biomass* **1990**, *21*, 239–255.

(9) Gunaseelan, V. N. Anaerobic digestion of biomass for methane production: A review. *Biomass and Bioenergy* **1997**, *13*, 83–114.

(10) Weng, X.; Ren, H.; Chen, M.; Wan, H. Effect of surface oxygen on the activation of methane on palladium and platinum surfaces. *ACS Catal.* **2014**, *4*, 2598–2604.

(11) Liander, H. The utilisation of natural gases for the ammonia process. *Trans. Faraday Soc.* **1929**, *25*, 462–472.

(12) York, A.; Xiao, T.; Green, M. Brief overview of the partial oxidation of methane to synthesis gas. *Top. Catal.* **2003**, *22*, 345–358.

(13) Tsang, S.; Claridge, J.; Green, M. Recent advances in the conversion of methane to synthesis gas. *Catal. Today* **1995**, *23*, 3–15.

(14) Enger, B. C.; Lødeng, R.; Holmen, A. A review of catalytic partial oxidation of methane to synthesis gas with emphasis on reaction mechanisms over transition metal catalysts. *Appl. Catal. A Gen.* **2008**, *346*, 1–27.

(15) Pakhare, D.; Spivey, J. A review of dry (CO_2) reforming of methane over noble metal catalysts. *Chem. Soc. Rev.* **2014**, *43*, 7813–7837.

(16) Kraus, P.; Lindstedt, R. P. Reaction class-based frameworks for heterogeneous catalytic systems. *Proc. Combust. Inst.* **2017**, *36*, 4329–4338.

(17) Kraus, P.; Lindstedt, R. P. Variational transition state theory based surface chemistry for the $C_2H_6/H_2/O_2/Pt$ system. *Energy and Fuels* **2017**, *31*, 2217–2227.

(18) Vincent, R.; Lindstedt, R. P.; Malik, N.; Reid, I.; Messenger, B. The chemistry of ethane dehydrogenation over a supported platinum catalyst. *J. Catal.* **2008**, *260*, 37–64.

(19) Warnatz, J. Resolution of gas phase and surface combustion chemistry into elementary reactions. *Proc. Combust. Inst.* **1992**, *24*, 553–579.

(20) Shustorovich, E.; Sellers, H. The UBI-QEP method: a practical theoretical approach to understanding chemistry on transition metal surfaces. *Surf. Sci. Rep.* **1998**, *31*, 5–119.

(21) Salciccioli, M.; Chen, Y.; Vlachos, D. G. Microkinetic modeling and reduced rate expressions of ethylene hydrogenation and ethane hydrogenolysis on platinum. *Ind. Eng. Chem. Res.* **2011**, *50*, 28–40.

(22) Warnatz, J.; Allendorf, M. D.; Kee, R. J.; Coltrin, M. E. A model of elementary chemistry and fluid mechanics in the combustion of hydrogen on platinum surfaces. *Combust. Flame* **1994**, *96*, 393–406.

(23) Ludwig, J.; Vlachos, D. G.; Van Duin, A. C. T.; Goddard, W. A. Dynamics of the dissociation of hydrogen on stepped platinum surfaces using the ReaxFF reactive force field. *J. Phys. Chem. B* **2006**, *110*, 4274–4282.

(24) Deutschmann, O.; Maier, L. I.; Riedel, U.; Stroemman, A. H.; Dibble, R. W. Hydrogen assisted catalytic combustion of methane on platinum. *Catal. Today* **2000**, *59*, 141–150.

(25) McDaniel, A. H.; Lutz, A. E.; Allendorf, M. D.; Rice, S. F. Effects of methane and ethane on the heterogeneous production of water from hydrogen and oxygen over platinum in stagnation flow. *J. Catal.* **2002**, *208*, 21–29.

(26) Zerkle, D. K.; Allendorf, M. D.; Wolf, M.; Deutschmann, O. Understanding homogeneous and heterogeneous contributions to the platinum-catalyzed partial oxidation of ethane in a short-contact-time reactor. *J. Catal.* **2000**, *196*, 18–39.

(27) Mantzaras, J.; Appel, C.; Benz, P. Catalytic combustion of methane / air mixtures over platinum: Homogeneous ignition distances in channel flow configurations. *Proc. Combust. Inst.* **2000**, *28*, 1349–1357.

(28) Hickman, D. A.; Schmidt, L. D. Synthesis gas formation by direct oxidation of methane over Pt monoliths. *J. Catal.* **1992**, *138*, 267–282.

(29) Ruiz, J. A. C.; Passos, F. B.; Bueno, J. M. C.; Souza-Aguiar, E. F.; Mattos, L. V.; Noronha, F. B. Syngas production by autothermal reforming of methane on supported platinum catalysts. *Appl. Catal. A Gen.* **2008**, *334*, 259–267.

(30) Deng, C.; Yang, W.; Zhou, J.; Liu, Z.; Wang, Y.; Cen, K. Catalytic combustion of methane, methanol, and ethanol in microscale combustors with Pt/ZSM-5 packed beds. *Fuel* **2015**, *150*, 339–346.

(31) Rostrup-Nielsen, J. R. Activity of nickel catalysts for steam of hydrocarbons. *J. Catal.* **1973**, *33*, 173–199.

(32) Horn, R.; Williams, K. A.; Degenstein, N. J.; Bitsch-Larsen, A.; Dalle Nogare, D.; Tupy, S. A.; Schmidt, L. D. Methane catalytic partial oxidation on autothermal Rh and Pt foam catalysts: Oxidation and reforming zones, transport effects, and approach to thermodynamic equilibrium. *J. Catal.* **2007**, *249*, 380–393.

(33) Nematollahi, B.; Rezaei, M.; Asghari, M.; Fazeli, A.; Lay, E. N.; Nematollahi, F. A comparative study between modeling and experimental results over rhodium supported catalyst in dry reforming reaction. *Fuel* **2014**, *134*, 565–572.

(34) Drif, A.; Bion, N.; Brahmi, R.; Ojala, S.; Pirault-Roy, L.; Turpeinen, E.; Seelam, P. K.; Keiski, R. L.; Epron, F. Study of the dry reforming of methane and ethanol using Rh catalysts supported on doped alumina. *Appl. Catal. A Gen.* **2015**, *504*, 576–584.

(35) Wehinger, G. D.; Eppinger, T.; Kraume, M. Detailed numerical simulations of catalytic fixed-bed reactors: Heterogeneous dry reforming of methane. *Chem. Eng. Sci.* **2015**, *122*, 197–209.

(36) Karakaya, C.; Deutschmann, O. Kinetics of hydrogen oxidation on Rh/Al_2O_3 catalysts studied in a stagnation-flow reactor. *Chem. Eng. Sci.* **2013**, *89*, 171–184.

(37) Karadeniz, H.; Karakaya, C.; Tischer, S.; Deutschmann, O. Mass transfer effects in stagnation flows on a porous catalyst: Water-gas-shift reaction over Rh/Al_2O_3. *Zeitschrift für Phys. Chemie* **2015**, *229*, 709–737.

(38) Karakaya, C.; Maier, L.; Deutschmann, O. Surface reaction kinetics of the oxidation and reforming of CH_4 over Rh/Al_2O_3 catalysts. *Int. J. Chem. Kinet.* **2016**, *48*, 144–160.

(39) Scarabello, A.; Dalle Nogare, D.; Canu, P.; Lanza, R. Partial oxidation of methane on Rh/ZrO_2 and Rh/Ce-ZrO_2 on monoliths: Catalyst restructuring at reaction conditions. *Appl. Catal. B Environ.* **2015**, *174-175*, 308–322.

(40) Filot, I. A. W.; Broos, R. J. P.; Van Rijn, J. P. M.; Van Heugten, G. J. H. A.; Van Santen, R. A.; Hensen, E. J. M. First-principles-based microkinetics simulations of synthesis gas conversion on a stepped rhodium surface. *ACS Catal.* **2015**, *5*, 5453–5467.

(41) Yang, N.; Medford, A. J.; Liu, X.; Studt, F.; Bligaard, T.; Bent, S. F.; Norskov, J. K. On the intrinsic selectivity and structure sensitivity of rhodium catalysts for C_2+ oxygenate production. *J. Am. Chem. Soc.* **2016**, *138*, 3705–3714.

(42) Reinke, M.; Mantzaras, J.; Schaeren, R.; Bombach, R.; Inauen, A.; Schenker, S. High-pressure catalytic combustion of methane over platinum: In situ experiments and detailed numerical predictions. *Combust. Flame* **2004**, *136*, 217–240.

(43) Appel, C.; Mantzaras, J.; Schaeren, R.; Bombach, R.; Inauen, A.; Tylli, N. N.; Wolf, M.; Griffin, T.; Winkler, D.; Carroni, R. Partial catalytic oxidation of methane to synthesis gas over rhodium: In situ Raman experiments and detailed simulations. *Proc. Combust. Inst.* **2005**, *30*, 2509–2517.

(44) Sui, R.; Mantzaras, J.; Bombach, R.; Denisov, A. Hetero-/homogeneous combustion of fuel-lean methane/oxygen/nitrogen mixtures over rhodium at pressures up to 12bar. *Proc. Combust. Inst.* **2017**, *36*, 4321–4328.

(45) Sui, R.; Mantzaras, J.; Bombach, R. A comparative experimental and numerical investigation of the heterogeneous and homogeneous combustion characteristics of fuel-rich methane mixtures over rhodium and platinum. *Proc. Combust. Inst.* **2017**, *36*, 4313–4320.

(46) Jones, W. P.; Lindstedt, R. P. Global reaction schemes for hydrocarbon combustion. *Combust. Flame* **1988**, *73*, 233–249.

(47) Spalding, D. B. *GENMIX: A general computer program for two-dimensional parabolic phenomena*, 1st ed.; Pergamon, 1977; pp 1–392.

(48) Patankar, S. V.; Spalding, D. B. *Heat and mass transfer in boundary layers: A general calculation procedure*, 2nd ed.; Intertext: London, 1970; pp 1–230.

(49) Coltrin, M. E.; Kee, R. J.; Rupley, F. M. Surface CHEMKIN: A general formalism and software for analyzing heterogeneous chemical kinetics at a gas-surface interface. *Int. J. Chem. Kinet.* **1991**, *23*, 1111–1128.

(50) Sui, R.; Mantzaras, J. Combustion stability and hetero-/homogeneous chemistry interactions for fuel-lean hydrogen/air mixtures in platinum-coated microchannels. *Combust. Flame* **2016**, *173*, 370–386.

(51) Coltrin, M. E.; Kee, R. J.; Miller, J. A. A mathematical model of the coupled fluid mechanics and chemical kinetics in a chemical vapor deposition reactor. *J. Electrochem. Soc.* **1984**, *131*, 425–434.

(52) Raja, L. L.; Kee, R. J.; Deutschmann, O.; Warnatz, J.; D. Schmidt, L. A critical evaluation of NavierStokes, boundary-layer, and plug-flow models of the flow and chemistry in a catalytic-combustion monolith. *Catal. Today* **2000**, *59*, 47–60.

(53) Leung, K. M.; Lindstedt, R. P. Detailed kinetic modeling of C_1–C_3 alkane diffusion flames. *Combust. Flame* **1995**, *102*, 129–160.

(54) Louloudi, S. Transported probability density function modeling of turbulent jet flames. Ph.D. thesis, Imperial College London, 2003.

(55) Lindstedt, R. P.; Waldheim, B. B. O. Modeling of soot particle size distributions in premixed stagnation flow flames. *Proc. Combust. Inst.* **2013**, *34*, 1861–1868.

(56) Lindstedt, R. P.; Skevis, G. Molecular growth and oxygenated species formation in laminar ethylene flames. *Proc. Combust. Inst.* **2000**, *28*, 1801–1807.

(57) Baulch, D. L.; Cobos, C. J.; Cox, R. a.; Esser, C.; Frank, P.; Just, T.; Kerr, J. a.; Pilling, M. J.; Troe, J.; Walker, R. W. et al. Evaluated kinetic data for combustion modelling. *J. Phys. Chem. Ref. Data* **1992**, *21*, 411–734.

(58) Baulch, D. L. Evaluated Kinetic Data for Combustion Modeling: Supplement II. *J. Phys. Chem. Ref. Data* **2005**, *34*, 757–1397.

(59) Quiceno, R.; Pérez-Ramírez, J.; Warnatz, J.; Deutschmann, O. Modeling the high-temperature catalytic partial oxidation of methane over platinum gauze: Detailed gas-

562 phase and surface chemistries coupled with 3D flow field simulations. *Appl. Catal. A*
563 *Gen.* **2006**, *303*, 166–176.

564 (60) Carl, S. A.; Nguyen, H. M. T.; Elsamra, R. M. I.; Nguyen, M. T.; Peeters, J. Pulsed laser
565 photolysis and quantum chemical-statistical rate study of the reaction of the ethynyl
566 radical with water vapor. *J. Chem. Phys.* **2005**, *122*, 114307.

567 (61) Klippenstein, S. J.; Miller, J. A.; Harding, L. B. Resolving the mystery of prompt CO_2:
568 The HCCO + O_2 reaction. *Proc. Combust. Inst.* **2002**, *29*, 1209–1217.

569 (62) Burke, M. P.; Chaos, M.; Ju, Y.; Dryer, F. L.; Klippenstein, S. J. Comprehensive H_2/O_2
570 kinetic model for high-pressure combustion. *Int. J. Chem. Kinet.* **2012**, *44*, 444–474.

571 (63) Rojo, J. M.; Belzunegui, J. P.; Sanz, J.; Guil, J. M. Hydrogen adsorption on rhodium
572 particles supported on strontium titanate as followed by ^{1}H NMR and microcalorimetry.
573 *J. Phys. Chem.* **1981**, *98*, 13631–13635.

574 (64) Thiel, P. A.; Yates Jr, J. T.; Weinberg, W. H. The interaction of oxygen with the
575 Rh(111) surface. *Surf. Sci.* **1979**, *82*, 22–44.

576 (65) Brass, S. G.; Ehrlich, G. Dissociative and molecular adsorption of methane on rhodium.
577 *Surf. Sci.* **1987**, *187*, 21–35.

578 (66) Jansen, M. M. M.; Scheijen, F. J. E.; Ashley, J.; Nieuwenhuys, B. E.; Niemantsver-
579 driet, J. W. Adsorption/desorption studies of CO on a rhodium(100) surface under
580 UHV conditions: A comparative study using XPS, RAIRS, and SSIMS. *Catal. Today*
581 **2010**, *154*, 53–60.

582 (67) Chang, C.-C.; Ho, J.-J. Dissociation of CO_2 on rhodium nanoclusters (Rh_13) in various
583 structures supported on unzipped graphene oxide - a DFT study. *Phys. Chem. Chem.*
584 *Phys.* **2015**, *17*, 11028–11035.

(68) Hickman, D. A.; Schmidt, L. D. Steps in CH_4 oxidation on Pt and Rh surfaces - High-temperature reactor simulations. *AIChE J.* **1993**, *39*, 1164–1177.

(69) Zum Mallen, M. P.; Williams, W. R.; Schmidt, L. D. Steps in Hydrogen Oxidation on Rhodium: Hydroxyl Desorption at High Temperatures. *J. Phys. Chem.* **1993**, *97*, 625–632.

(70) Wang, C. B.; Yeh, C. T. Calorimetric study on oxidation of alumina supported rhodium by dioxygen. *J. Mol. Catal. A-Chemical* **1997**, *120*, 179–184.

(71) Inderwildi, O. R.; Lebiedz, D.; Deutschmann, O.; Warnatz, J. Coverage dependence of oxygen decomposition and surface diffusion on rhodium (111): A DFT study. *J. Chem. Phys.* **2005**, *122*, 034710.

(72) Bonanni, M. Detailed modelling of heterogeneous chemistry on palladium and platinum. Ph.D. thesis, Imperial College London, 2011.

(73) Guil, J.; Herrero García, J.; Ruiz Paniego, A.; Trejo Menayo, J. Gas/surface titration microcalorimetry. Energetics of oxygen adsorption on supported iridium catalysts. *Top. Catal.* **2002**, *19*, 313–321.

(74) Díaz, E.; Ordóñez, S.; Vega, A.; Coca, J. Influence of catalyst treatments on the adsorption properties of γ-Al_2O_3 supported Pt, Rh and Ru catalysts. *Microporous Mesoporous Mater.* **2005**, *77*, 245–255.

(75) Rut'kov, E. V.; Kuz'michev, a. V.; Gall', N. R.; Rut'kov, E. V.; Kuz'michev, a. V.; Gall', N. R. Carbon interaction with rhodium surface: Adsorption, dissolution, segregation, growth of graphene layers. *Phys. Solid State* **2011**, *53*, 1092–1098.

(76) Baraldi, A.; Gregoratti, L.; Comelli, G.; Dhanak, V. R.; Kiskinova, M.; Rosei, R. CO adsorption and CO oxidation on Rh(100). *Appl. Surf. Sci.* **1996**, *99*, 1–8.

(77) Dulaurent, O.; Chandes, K.; Bouly, C.; Bianchi, D. Heat of adsorption of carbon monoxide on a Pd/Rh three-way catalyst and on a Rh/AlO solid. *J. Catal.* **2000**, *192*, 262–272.

(78) Smedh, M.; Beutler, A.; Borg, M.; Nyholm, R.; Andersen, J. N. Determination of the coverage dependent isosteric heat of adsorption of CO on Rh(111) by high resolution core level photoemission. *Surf. Sci.* **2001**, *491*, 115–123.

(79) He, R.; Kusaka, H.; Mavrikakis, M.; Dumesic, J. A. Microcalorimetric, infrared spectroscopic and DFT studies of CO adsorption on Rh and Rh-Te catalysts. *J. Catal.* **2003**, *217*, 209–221.

(80) Savargaonkar, N.; Khanra, B. C.; Pruski, M.; King, T. S. Influence of hydrogen chemisorption on the surface composition of Pt-Rh/Al_2O_3 catalysts. *J. Catal.* **1996**, *162*, 277–283.

(81) Hellsing, B.; Kasemo, B.; Ljungström, S.; Rosén, A.; Wahnström, T. Kinetic model and experimental results for H_2O and OH production rates on Pt. *Surf. Sci.* **1987**, *189-190*, 851–860.

(82) Warnatz, J.; Maas, U.; Dibble, R. W. *Combustion: Physical and chemical fundamentals, modeling and simulation, experiments, pollutant formation*, 4th ed.; Springer-Verlag: Berlin, 2006; p 378.

Table of Contents figure